Journal of Water Process Engineering 71 (2025) 107216

Contents lists available at ScienceDirect

Journal of Water Process Engineering

journal homepage: www.elsevier.com/locate/jwpe

Improved photocatalytic behavior of Ag-WO_3/$BiVO_4$ nanocomposite towards the removal of eosin yellow (EY) under visible light

Suresh Kumar Pandey [a,b], Prerna Sarwan [a], Dhanesh Tiwary [a,*], Mohammad Salman [c]

[a] Department of Chemistry, Indian Institute of Technology (Banaras Hindu University), Varanasi 221005, India
[b] Faculty of Chemical Engineering and Technology, University of Zagreb, Zagreb HR-10000, Croatia
[c] Department of Chemistry and Materials Science Innovation & Modelling (MaSIM) Research Focus Area, Faculty of Natural and Agricultural Sciences, North-West University, Private Bag X2046, Mmabatho 2735, South Africa

ARTICLE INFO

Editor: Akeem Oladipo

Keywords:
Photocatalysis
Eosin yellow
Band gap
Active species
Quantum yield

ABSTRACT

The photocatalytic removal of organic pollutants from wastewater is recognized as an economically viable and environmentally friendly technique. In this study, we successfully synthesized an Ag-WO_3/$BiVO_4$ (ABvW) nanocomposite photocatalyst that demonstrates exceptional efficiency in the photocatalytic degradation of eosin yellow (EY) dye. The synthesized photocatalysts were comprehensively characterized using various techniques, including BT-XRD, FE-SEM, XPS, BET and UV-DRS, to confirm their structural and optical properties.

The photocatalytic degradation of EY was conducted under LED light illumination, and our findings reveal that the ABvW nanocomposite exhibits superior photocatalytic performance, achieving nearly 94 % dye removal within 70 min with a high Quantum yield (QY) value. This performance is significantly higher than that of pure WO_3, $BiVO_4$, or Ag/WO_3 samples individually. The enhanced photocatalytic activity of the ABvW nanocomposite is likely due to the effective suppression of charge recombination, increased specific surface area, and improved redox potential of the composite material, all of which contribute to the superior photocatalytic performance of the ABvW nanocomposite.

1. Introduction

With the rapid pace of industrial development and ongoing population growth, global resource consumption has surged, leading to a significant depletion of non-renewable resources [1]. Among the pressing environmental concerns, water pollution stands out as one of the most critical, primarily driven by the expanding population and the increasing discharge of waste from the textile and chemical industries [2]. A major contributor to environmental contamination, particularly in water bodies, is the presence of non-biodegradable organic pollutants such as dyes, pesticides, phenolic derivatives, personal care products, and pharmaceuticals [3–6]. These compounds are highly problematic because they persist in the environment, degrade slowly and pose serious health risks due to their carcinogenic, teratogenic, mutagenic, and toxic properties [7,8].

Several physical and chemical methods, including ion exchange, coagulation, electrochemical oxidation, and ultrafiltration, have been explored to mitigate these pollutants. However, many of these approaches are constrained by the need for specialized equipment, high operational costs, and complex manual procedures [9,10]. In response to these limitations, photocatalysis has recently emerged as an efficient, eco-friendly, and cost-effective technique for degrading organic and toxic pollutants in both air and water under solar irradiation [11–14]. Heterogeneous photocatalysis, in particular, has attracted considerable attention because it can break down hazardous organic pollutants into harmless end products, such as CO_2 and H_2O, in the presence of sunlight, making it both environmentally benign and economically viable [15,16].

Among the photocatalysts studied, titanium dioxide (TiO_2) has been the most extensively investigated due to its commercial availability, strong photocatalytic activity, non-toxicity, good chemical stability, and low cost. However, TiO_2 has a broad bandgap energy of 3.2 eV, which limits its responsiveness to the ultraviolet portion of the solar spectrum—accounting for <4 % of sunlight—thereby restricting its practical applicability [17,18]. Currently, the development of visible-light-driven photocatalysts is a critical area of research [19].

Bismuth vanadate ($BiVO_4$) has garnered significant interest among these advanced photocatalysts because of its narrow band gap (2.4 eV),

* Corresponding author.
E-mail address: dtiwari.apc@itbhu.ac.in (D. Tiwary).

https://doi.org/10.1016/j.jwpe.2025.107216
Received 27 November 2024; Received in revised form 22 January 2025; Accepted 7 February 2025
Available online 13 February 2025

excellent visible-light responsiveness, and non-toxic nature [20]. However, the photocatalytic efficiency of pure $BiVO_4$ is hindered by the rapid recombination of photogenerated electron-hole pairs. To overcome this limitation, $BiVO_4$ has been modified through metal or metal oxide doping or by forming composites with other metal or non-metal oxides, which enhances the separation efficiency of electron-hole pairs, thereby improving photocatalytic performance [21,22].

Similarly, tungsten trioxide (WO_3), an n-type semiconductor, has been extensively studied as a visible-light-responsive photocatalyst. WO_3 is a chemically stable, non-toxic material with a band gap of 2.6–3.0 eV, making it highly effective in absorbing solar radiation [23]. However, the small band gap of WO_3 also leads to a high recombination rate of photogenerated electron-hole pairs, which limits its photocatalytic efficiency [24]. To address this challenge, noble metals such as silver (Ag) are loaded onto WO_3 to improve electron-hole separation, thereby enhancing photocatalytic activity [25].

In this study, a composite of Ag-WO_3/$BiVO_4$ was synthesized using a hydrothermal method, with the aim of modifying the surface and the electronic properties of $BiVO_4$ nanoparticles through the incorporation of the Ag-WO_3 matrix. The photocatalytic performance of this composite was assessed by its ability to degrade eosin yellow (EY) under visible light irradiation. Notably, the Ag-WO_3/$BiVO_4$ photocatalyst exhibited significantly enhanced photocatalytic activity compared to its individual components- $BiVO_4$, WO_3, and Ag-WO_3- highlighting the synergistic effects of the composite structure in improving photocatalytic efficiency.

2. Experimental

2.1. Materials and methods

Bismuth (III) nitrate pentahydrate ($Bi(NO_3)_3.5H_2O$; SRL), ammonium metavanadate (NH_4VO_3; Molychem), ethylene glycol (Merck), sodium tungstate (Na_2WO_4; SRL), hydrochloric acid (HCl), oxalic acid ($H_2C_2O_4$; Merck), silver nitrate ($AgNO_3$; Merck), sodium borohydride ($NaBH_4$; Merck), eosin yellow (EY) were used in this study. All chemicals were used as received from the suppliers, without any further purification or modification.

2.1.1. Synthesis of $BiVO_4$

To synthesize $BiVO_4$ (Bv), aqueous solutions of $Bi(NO_3)_3.5H_2O$ and NH_4VO_3 were mixed in a 1:1 M ratio. A 0.5 M aqueous ethylene glycol solution was then added to the suspension. The resulting mixture was transferred into a 200 mL Teflon-lined stainless-steel autoclave, which was sealed tightly. The autoclave was placed in a hot air oven at 160 °C for 12 h. Afterwards, the sample was centrifuged and washed throughly with distilled water and ethanol. The obtained solid material was dried at 70 °C, and the resulting yellow powder was calcined at 500 °C for 1 h in a muffle furnace.

2.1.2. Synthesis of WO_3

An appropriate amount of Na_2WO_4 (0.5 M) was dissolved in 37.5 mL of distilled water using a magnetic stirrer. Then 0.5 mL of a 2 M HCl solution was added dropwise to the reaction mixture. Thereafter, a solution of 0.413 g of $H_2C_2O_4$ in 75 mL of distilled water was added to the precursor solution. The mixed solution was then transferred into a hydrothermal synthesis reactor and heated at 90 °C for 3 h in an oven. The obtained sample was then centrifuged, washed with water, and dried well. The dried sample is WO_3 (W).

2.1.3. Synthesis of Ag-WO_3

1.16 g of the prepared WO_3 was dispersed in 50 mL of distilled water by ultrasonication for 60 min. Then, 0.058 g of $AgNO_3$ (5 % by weight of WO_3) was added to the dispersion, and the mixture was stirred vigorously. An aqueous solution of $NaBH_4$ (0.5 M% of $AgNO_3$) was added dropwise to the reaction mixture, which was continuously stirred for 2 h. Afterwards, the resulting sample was centrifuged and washed with distilled water and ethanol. The obtained solid sample was dried in an oven at 70 °C. The resulting powder is Ag-WO_3 (AW) nanocomposite.

2.1.4. Synthesis of Ag-WO_3/$BiVO_4$

For the synthesis of the Ag-WO_3/$BiVO_4$ (ABvW) nanocomposite, appropriate amounts of $BiVO_4$ (Bv) and Ag-WO_3 (AW) (30 % by weight of $BiVO_4$) were dispersed in 50 mL of distilled water by ultrasonication for 1 h. The sample solution was then stirred for 4 h. The resulting mixture was centrifuged, washed, and dried in an oven at 70 °C.

2.2. Characterization

The synthesized materials were analyzed by using various characterization techniques to assess their structural, morphological, and optical properties. The crystallinity and phase purity of the samples were examined by bench-top X-ray diffraction (BT-XRD; Rigaku Miniflex 600; $\lambda = 1.54$ Å) equipped with Cu Kα radiation. A field-emission scanning electron microscope (FESEM; Nova Nano SEM 450) coupled with an energy dispersive X-ray spectrometer (EDS; Team Pegasus Integrated EDS-EBSD with Octane Plus and Hikari Pro Dectector) was employed to investigate the surface morphology and elemental composition. The chemical states of the elements in the samples were determined using X-ray photoelectron spectroscopy (XPS; K-Alpha). The specific surface area of the samples was evaluated using the Brunaur-Emmett-Teller (BET) method, with measurements performed on a BELSORP MAX II & BELCAT-II surface area analyzer. To investigate the optical properties of the powdered samples, spectra were recorded on a ultraviolet-visible diffuse reflectance spectrophotometer (UV–Vis DRS; Shimadzu Pharmaspecs UV-1700).

2.3. Photocatalytic efficiency

The photocatalytic performance of the prepared samples was evaluated by the removal of eosin yellow (EY) dye under exposure to LED lights (2 × 14 W). The photocatalytic experiment was carried out in a beaker, where a mixed solution of 20 ppm EY and 0.1 g/L of the catalyst was prepared. Prior to light exposure, the mixed solution was stirred in the dark for 60 min to achieve adsorption-desorption equilibrium. Afterward, the solution was irradiated with LED lights, and at every 10-min interval, 2 mL of the solution was withdrawn from the beaker to record the UV–Visible spectra. The decrease in the absorbance of EY ($\lambda = 518$ nm) over time determines the activity of the catalysts. The degradation percentage of EY was calculated by using the equation:

$$(\%)Removal = \frac{A_0 - A_t}{A_0}$$

Where A_0 and A_t are the absorbance of EY at time zero and after time t [26].

In order to determine the reactive species formed during the course of photocatalytic reaction, a trapping experiment was performed using equi-molar concentrations (0.5 mM) of potassium iodide (KI), Isopropyl alcohol (IPA), and p-benzoquinone (PBQ) to trap holes (h^+), hydroxide radicals ($^{\bullet}OH$), and anionic superoxide radicals ($O_2^{\bullet-}$) respectively.

3. Results and discussion

3.1. Crystal structure analysis

The samples were characterized through BT-XRD to analyze their crystallinity and phase purity. The XRD results (Fig. 1) show that the prepared samples are crystalline in nature. The peaks of Bv and W are well indexed, corresponding to the monoclinic crystal phase of $BiVO_4$ (ICSD reference code number: 01–075-2480) and WO_3 (ICSD reference code number: 01–072-0677) respectively. The formation of composites was confirmed by the appearance of the characteristic peaks of both

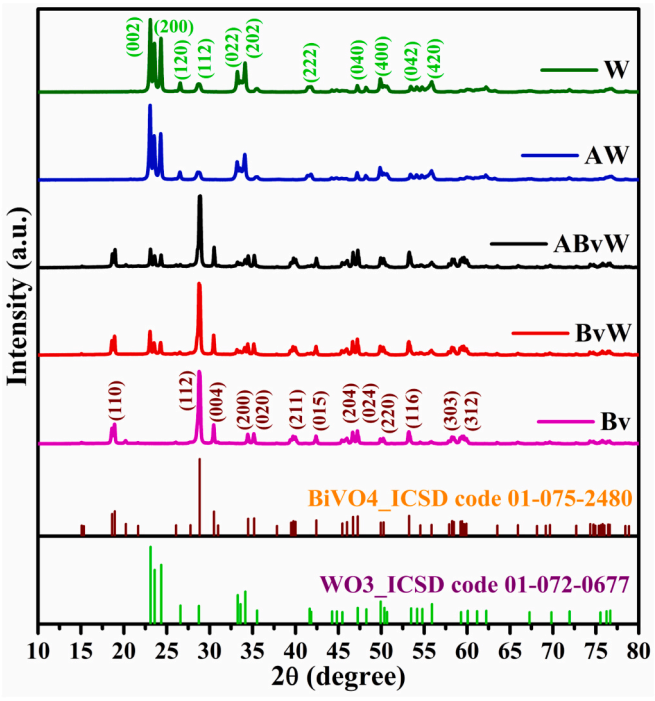

Fig. 1. XRD patterns of the synthesized samples (Bv, BvW, ABvW, AW, and W).

WO_3 and $BiVO_4$ in BvW and ABvW samples. No significant peaks corresponding to silver were observed in the AW and ABvW samples, likely due to the low percentage of silver loading in these samples.

3.2. Composition and chemical state analysis

Fig. 2 displays the XPS spectrum of the corresponding elements of ABvW sample. Fig. 2a presents the 4f spectra of Bi, where the two peaks appearing at 158.83 and 164.11 eV are attributed to the $4f_{7/2}$ and $4f_{5/2}$ states of Bi^{+3}, respectively. The core level spectrum of V 2p shows a doublet peak at binding energies of 516.56 eV and 524.10 eV, which correspond to the V $2p_{3/2}$ and V $2p_{1/2}$ states of VO_4^{-3}, respectively (Fig. 2b) [27]. In Fig. 2c, the two peaks of W 4f located at 36.15 eV and 37.83 eV are assigned to the $4f_{7/2}$ and $4f_{5/2}$ states of W^{+6}, respectively. The peaks around 529.36 eV and 530.29 eV are due to the presence of lattice oxygen, while another peak of oxygen at 531.43 eV is attributed to atmospheric moisture adsorbed on the surfaces of the sample (Fig. 2d) [28–30]. A doublet peak of Ag appears at 367.6 eV and 373.6 eV, corresponding to the Ag $3d_{5/2}$ and Ag $3d_{3/2}$, respectively (Fig. 2e). The binding energy difference of 6 eV between the 3d doublet peaks of Ag confirms the presence of metallic silver [25,31]. The atomic percentage of elemental silver, as calculated using CasaXPS software, was found to be 2.77 %. The fully scanned XPS survey spectrum (Fig. 2f) confirms the presence of all the relevant elements in the ABvW nanocomposite.

3.3. Morphological analysis

The surface morphologies of the prepared samples were analyzed using FE-SEM, and the results are presented in Fig. 3. In Fig. 3a, the FE-SEM image of sample Bv reveals that the $BiVO_4$ particles exhibit an irregular plate-like structure. Fig. 3b demonstrates that the morphology of pure WO_3 is distinctly cubic. Fig. 3c and d depict a mixed morphology, representing both $BiVO_4$ and WO_3, indicating the successful formation of the nanocomposites. The cubic morphology offers a larger surface area for reactions compared to the plate-like structure, which plays a crucial role in enhancing the photocatalytic efficiency of the nanocomposites. Additionally, the elements present in the corresponding composite samples were confirmed through EDS spectra (Fig. SI-1),

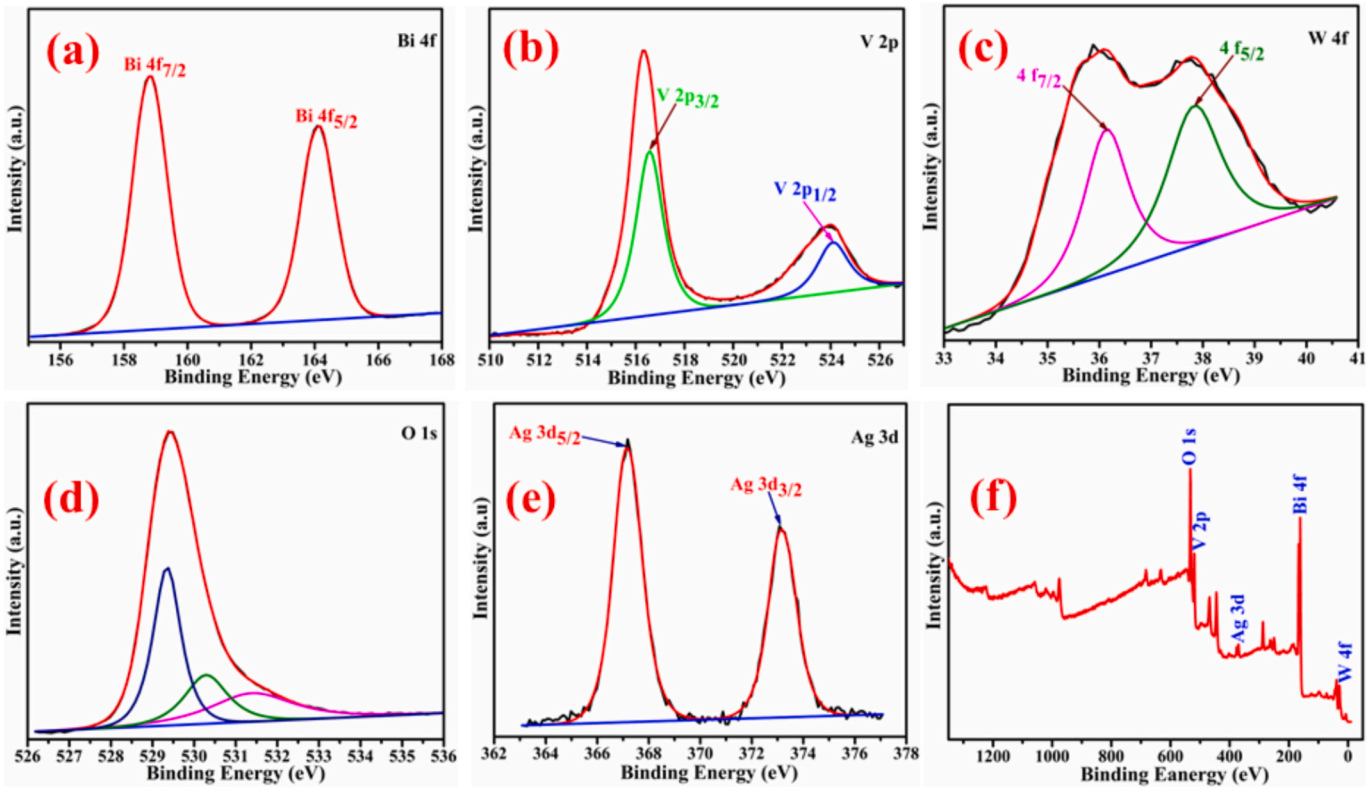

Fig. 2. XPS spectrum of (a) Bismuth, (b) Vanadium, (c) Tungsten, (d) Oxygen, and (e) Silver, (f) XPS survey spectrum of ABvW.

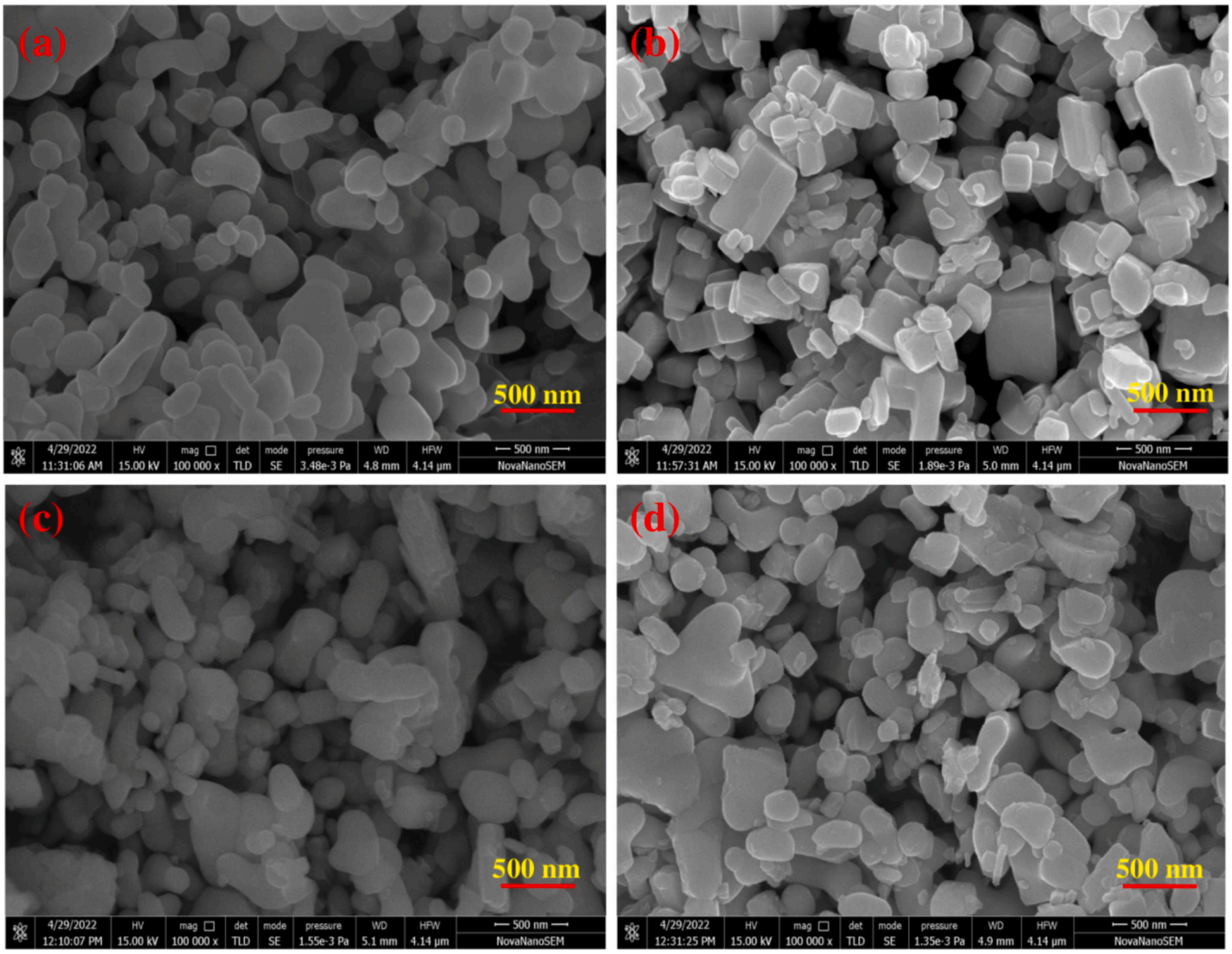

Fig. 3. FE-SEM images of (a) BV, (b) W, (c) BvW, and (d) ABvW.

verifying the formation of the desired materials. Fig. SI-2a shows the TEM image of ABvW, revealing small dark spot-like silver particles dispersed over the agglomerated WO_3 and $BiVO_4$ particles. The presence of discontinuous diffraction ring in the SAED pattern (Fig. SI-2b) reveals the polycrystalline nature of the composite.

3.4. Optical band-gap analysis

Fig. 4 displays the optical band gap energy for the Bv, W, AW, BvW, and ABvW samples. The band gap energies were calculated from the absorbance data obtained via UV-DRS, using the Tauc and Davis-Mott relation [32] –

$$(\alpha h\nu)^{\frac{1}{n}} = (h\nu - E_g)$$

Here, the symbol "Eg" represents the optical band gap energy, "α" is the molar absorption coefficient, "hν" is the energy of the incident photon, and the exponent "n" in the equation represent the mode of transition. For a direct transition, n = ½, while for the indirect transition, $n = 2$. The calculated band gap energies were found to be 2.46, 2.92, 2.83, 2.55, and 2.53 eV for the Bv, W, AW, BvW, and ABvW samples respectively.

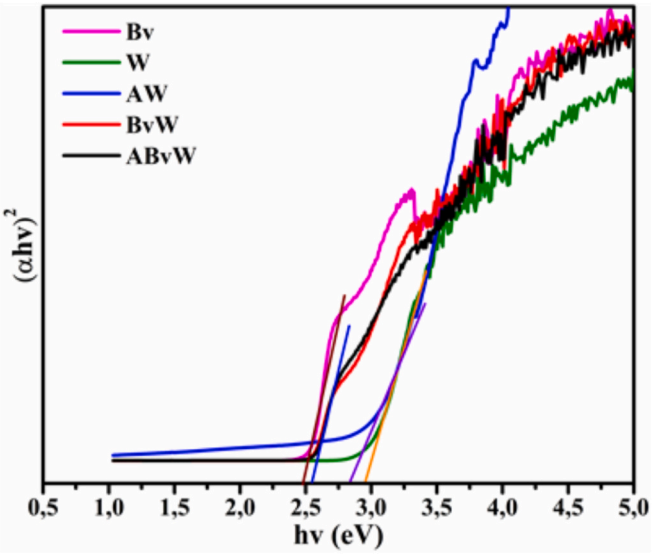

Fig. 4. Tauc plots of Bv, W, AW, BvW, and ABvW.

3.5. Determination of specific surface area of the materials

The specific surface area and porosity of the samples were determined using the BET technique. Figs. 5(a-c) present the N_2 adsorption-desorption isotherms for the Bv, W, and ABvW samples, respectively. The figures show typical type IV adsorption curves with H3-type hysteresis loops, indicating the presence of mesoporosity in the samples [33]. The average pore diameter of the samples, estimated using the BJH method, ranges from 35 to 40 nm (as shown in the insets of Fig. 5). The measured BET surface areas of the Bv, W, and ABvW samples are 4.69 m^2/g, 6.57 m^2/g, and 6.46 m^2/g, respectively. The slight increase in surface area of Bv upon introducing WO_3 into the nanocomposite offers more active sites for photocatalytic reactions, thereby enhancing its overall efficiency.

4. Analysis of photocatalytic activity

The photocatalytic activity of the samples was evaluated using Eosin Yellow (EY) dye under visible light irradiation. The results of the photocatalytic experiments are shown in Fig. 6. From the data, it is evident that the characteristic absorbance peak of EY nearly disappears in the presence of the ABvW catalyst after 70 min of irradiation (Fig. 6a). We selected 70 min as the standard irradiation time for testing all other samples. Fig. 6b depicts the absorbance spectra of EY degraded by the BvW photocatalyst. The UV–Vis absorbance spectra of EY decomposed by other photocatalytic samples are provided in the supplementary information (refer Fig. SI-3).

Fig. 6c presents a comparative plot of photocatalytic degradation (%) versus time for the EY dye using various catalysts. It can be seen that the ABvW catalyst, under LED light, exhibited the highest efficiency, degrading almost 94 % of the EY dye. Under the same conditions, the Bv, W, AW, and BvW catalysts degraded 46.81 %, 17.31 %, 42.56 %, and 67.54 % of the dye, respectively. Moreover, the adsorption of EY over ABvW in the dark is approximately 11 %. The superior photocatalytic performance of ABvW is likely attributed to its enhanced specific surface area and improved charge separation, which minimizes recombination. The kinetic analysis of the degradation process (Fig. 6d) shows that it follows pseudo-first-order kinetics. The rate constant for EY degradation over ABvW (2.88×10^{-2} min^{-1}) is the highest among all the samples.

The stability of a photocatalyst is crucial for its practical application [34,35]. To assess this, we conducted recyclability tests for our most effective sample, ABvW. Remarkably, we observed only a 6 % decrease in the degradation efficiency of the EY dye after five cycles (Fig. SI-4). This result demonstrates that our photocatalyst, ABvW, exhibits excellent stability under visible light irradiation.

To effectively capture the photocatalytic performance we have calculated the Quantum Yield (QY) of the photocatalyst by using Eq. [36]:

$$QY = \frac{Decomposition\ rate\ (molecule/second)}{Photon\ flux\ (photon/second)}$$

While QY is an effective metric for assessing photocatalytic performance, it does not account for the efficiency relative to the mass of the photocatalyst used [37]. To address this limitation, the space time yield (STY) is introduced:

$$STY = \frac{Quantum\ yield\ (molecule/photon)}{Mass\ of\ photocatalyst\ (mg)}$$

STY provides a more meaningful representation of photocatalytic efficiency per unit mass of catalyst [38].

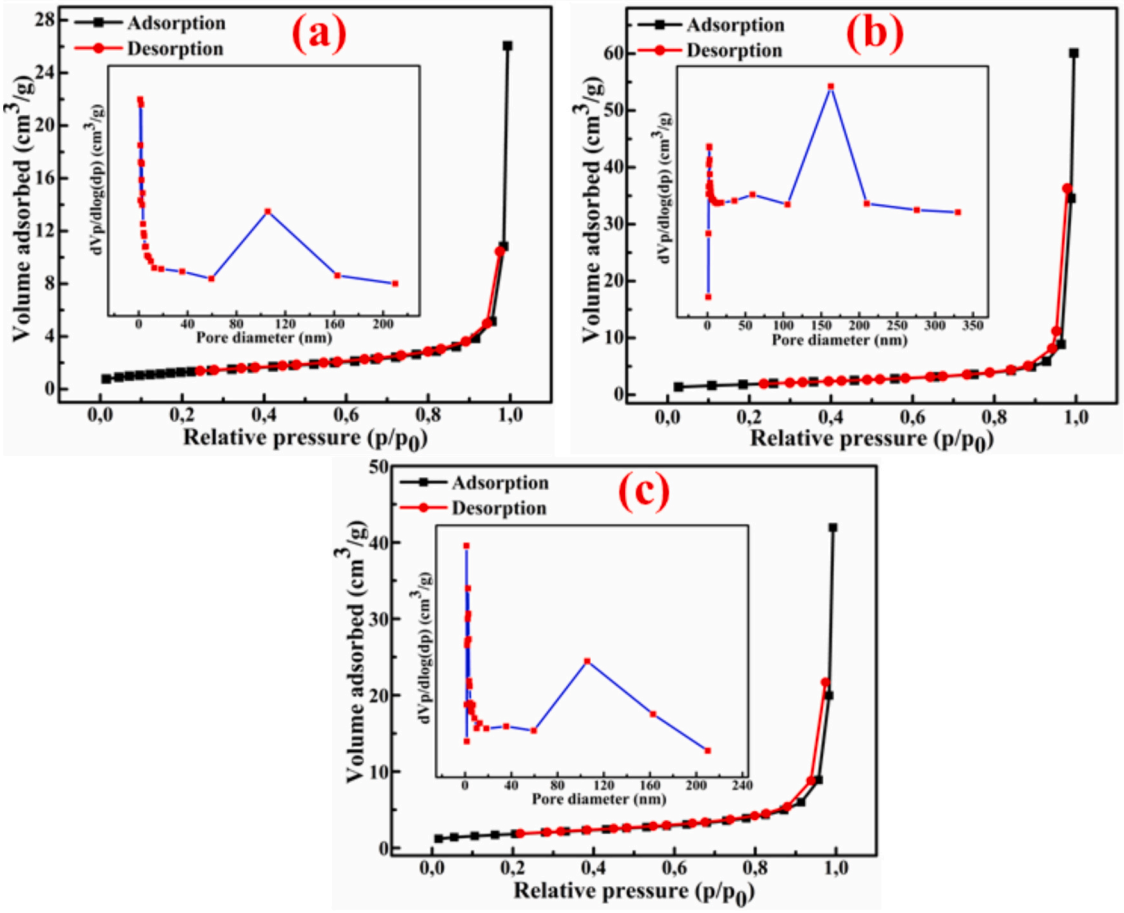

Fig. 5. N_2 adsorption-desorption isotherms and BJH plots (inserts) of (a) Bv, (b) W, and (c) ABvW.

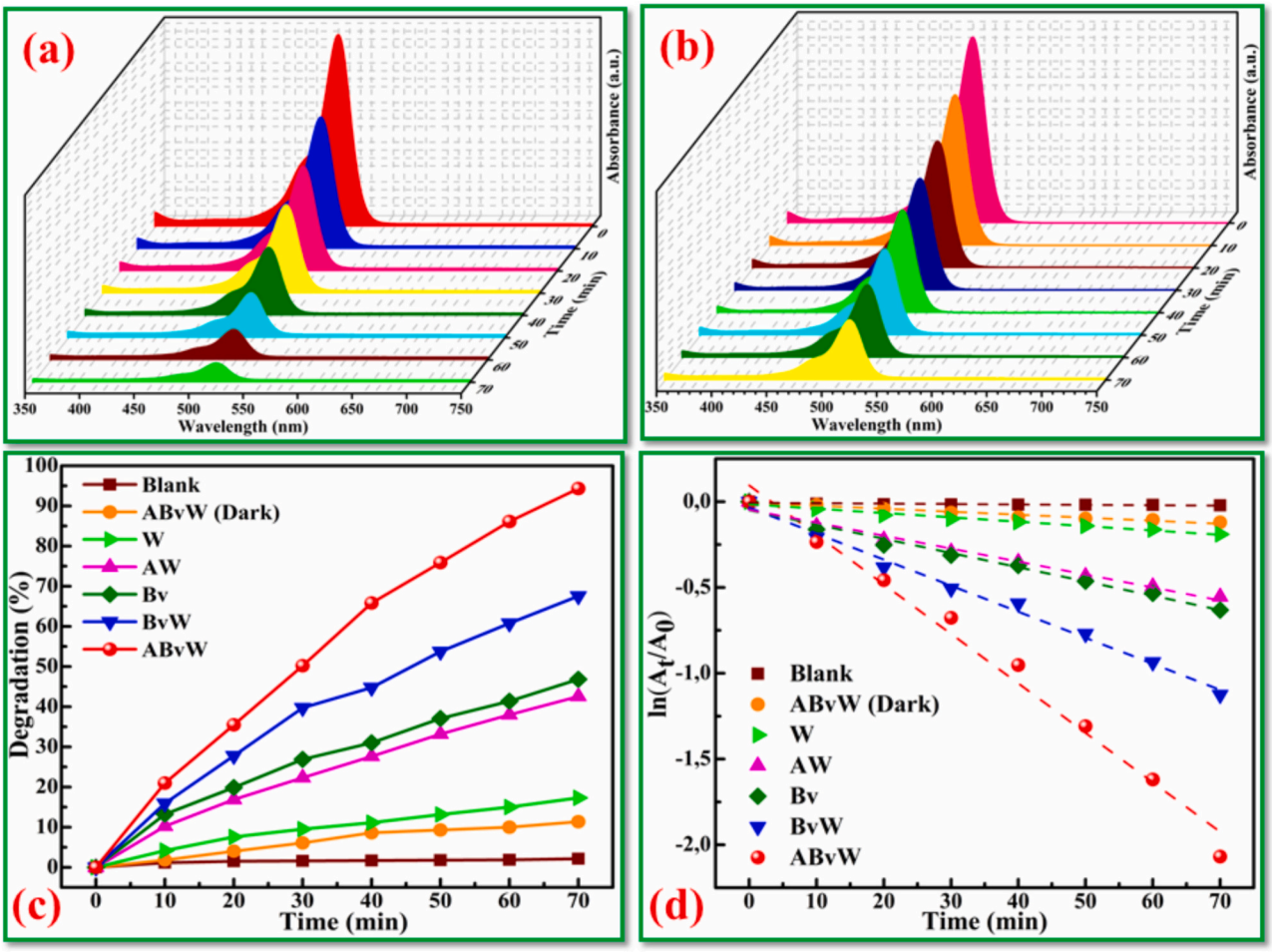

Fig. 6. (a), (b) Absorption spectra of EY under illumination over ABvW, BvWphotocatalysts respectively, (c) comparative degradation percentages of EY across various samples, and (d) Kinetic plots illustrating the degradation of EY degradation by different samples.

To further enhance performance evaluation, a figure of merit (FOM) has also been proposed. This FOM provides a unified metric that integrates key performance aspects of photocatalysts under relevant conditions, offering a standardized basis for evaluating and comparing catalytic efficacy across various applications and catalyst compositions [39].

The Figure of Merit (FOM) has been calculated by using the following formula:

$$FOM = \frac{Product\ obtained\ (L)}{Mass\ of\ catalyst\ (g) \times time(h) \times Energy\ consumption(Wh/\mu mol)}$$

The calculated values of the Quantum Yield (QY), Space Time Yield (STY), and Figure of Merit (FOM) for our sample are compared with those from previous studies on the photocatalytic degradation of EY (refer Table 1). It can be clearly seen from Table 1 that QY, STY, and FOM of our Ag-WO_3/$BiVO_4$ (ABvW) catalyst are much higher than those reported in previous studies.

Table 1
Comparison of key parameters: Current study vs. previous research on EY degradation.

Sr. No.	Photocatalysts	Kinetic Rx^n rate (μmol g^{-1} h^{-1})	QY (molecules $photon^{-1}$)	STY (molecules $photon^{-1}$ mg^{-1})	FOM (mol L $h^{-1}J^{-1}g^{-1}$)	Ref.
1.	Er-ZnO	1.17×10^{1}	3.342×10^{-7}	6.6843×10^{-9}	1.019×10^{-12}	[40]
2.	ZnO/SnO_2	1.32×10^{1}	7.518×10^{-7}	7.5182×10^{-9}	1.146×10^{-12}	[41]
3.	AgBr/ZnO	1.08×10^{1}	8.378×10^{-7}	5.5855×10^{-9}	2.417×10^{-12}	[42]
4.	Co-ZnO/g-C_3N_4	9.25×10^{0}	4.884×10^{-7}	4.8837×10^{-9}	5.71×10^{-13}	[43]
5.	Zn_2SnO_4/V_2O_5	8.86×10^{0}	9.143×10^{-7}	4.5714×10^{-9}	1.094×10^{-12}	[44]
6.	Co-ZrO_2/MWCNTs	8.38×10^{0}	4.426×10^{-7}	4.4259×10^{-9}	5.175×10^{-13}	[45]
7.	TiO_2/Ag_2S	2.32×10^{1}	3.593×10^{-7}	1.1976×10^{-8}	2.15×10^{-12}	[46]
8.	NiO/WO_3	9.15×10^{-1}	1.416×10^{-7}	4.7204×10^{-10}	1.695×10^{-13}	[47]
9.	Ag-ZnO	6.23×10^{1}	3.857×10^{-6}	3.8567×10^{-8}	1.385×10^{-11}	[48]
10.	Glass/Ag-TiO_2	2.33×10^{1}	1.200×10^{-6}	1.2004×10^{-8}	7.185×10^{-13}	[49]
11.	ZnO/CuO	3.34×10^{0}	8.608×10^{-8}	1.7216×10^{-9}	1.030×10^{-13}	[50]
12.	Ag-WO_3/$BiVO_4$	2.35×10^{2}	6.495×10^{-6}	6.4946×10^{-7}	2.011×10^{-10}	This work

Note: The λmax values are utilized as reported in the literature. In instances where λ_{max} values are not specified, we have assumed a value of 430 nm for solar/visible light ($\lambda > 400$ nm) and a lamp power of 150 W.

5. Active species analysis

The results of the trapping experiments, presented in Fig. 7, provide compelling evidence of how different scavengers modulate the photocatalytic degradation of EY to varying extents. As depicted in the figure, the ABvW photocatalyst (without any scavengers) achieves approximately 77 % degradation of EY within 50 min. However, when specific scavengers (PBQ, KI, IPA) are added under the same conditions, the degradation rate is significantly reduced. The extent of suppression varies, with IPA causing the most significant reduction, while PBQ has the least impact. These observations strongly suggest that the photocatalytic degradation of EY is primarily driven by $^{\bullet}OH$ and h^+ species. The relative contribution of each reactive species to the overall degradation follows the order: $^{\bullet}OH > h^+ > O_2^{\bullet-}$.

6. Photocatalytic mechanism

The enhanced photocatalytic degradation efficiency of the ABvW heterostructure can be attributed to the proposed mechanism, which follows a typical type-II heterojunction model, as illustrated in Fig. 8. The positions of the valence band (VB) and conduction band (CB) edges for WO_3 and $BiVO_4$ were determined using eqs. (5) and (6) from our previous work [3].

$$E_{VB} = \chi - E^e + 0.5E_g$$

$$E_{CB} = \chi - E^e - 0.5E_g$$

As depicted in the figure, the ABvW heterostructure adopts a type-II band alignment. Upon irradiation with LED light, electrons in the valence bands of both WO_3 and $BiVO_4$ are excited, transitioning to their respective conduction bands, thereby leaving holes in the valence bands. The excited electrons in the CB of $BiVO_4$ are transferred to Ag, which acts as an electron sink, facilitating their migration to the CB of WO_3. Simultaneously, the holes (h^+) in the VB of WO_3 are transferred to the VB of $BiVO_4$, driven by electrostatic forces.

As a result, electrons accumulate in the CB of WO_3, while holes populate the VB of $BiVO_4$. This spatial separation of photo-generated charge carriers reduces the likelihood of electron-hole recombination, thereby enhancing photocatalytic efficiency. Furthermore, the VB edge of $BiVO_4$ (2.77 eV) is more positive than the oxidation potential of the hydroxyl radical ($^{\bullet}OH$) at 2.4 eV, faciliting the generation of highly reactive $^{\bullet}OH$ radicals at the VB of $BiVO_4$. These $^{\bullet}OH$ radicals play a significant role in the photocatalytic degradation of eosine yellow (EY) dye. Fig. SI-5 presents a plausible oxidative degradation pathway for EY, where its mineralization occurs through the structural cleavage of large compounds, initiated by $^{\bullet}OH$ radicals [51,52].

Conversely, the CB edges of both $BiVO_4$ and WO_3 (0.31 eV and 0.61 eV, respectively) are less negative than the reduction potential of $O_2/O_2^{\bullet-}$ (−0.33 eV). Consequently, the formation of superoxide radicals ($O_2^{\bullet-}$) is energetically unfavorable, leading to negligible $O_2^{\bullet-}$ radical generation during photocatalysis, as confirmed by the trapping experiments. This selective radical generation, combined with efficient charge separation, is responsible for the superior photocatalytic performance of the ABvW heterostructure.

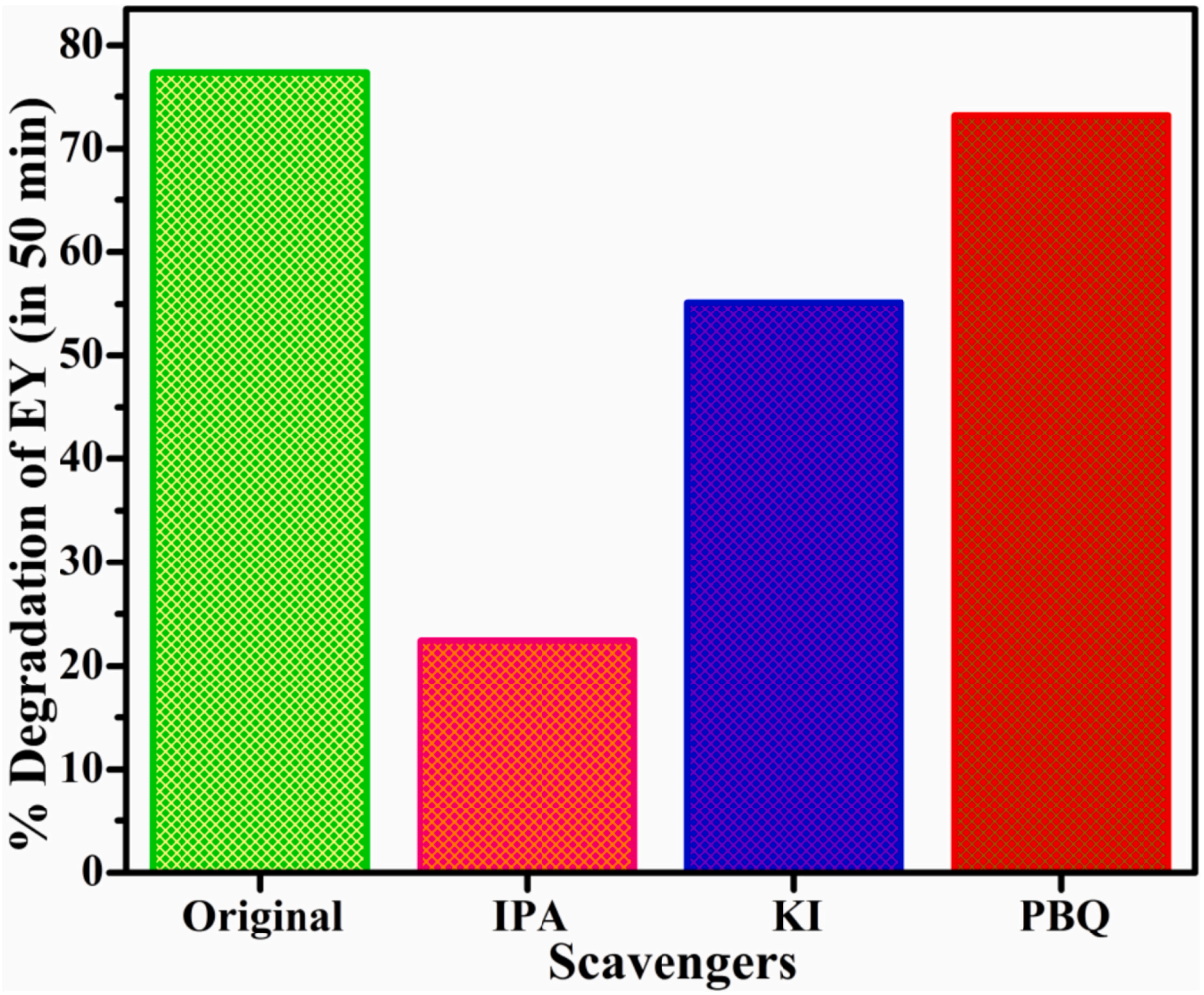

Fig. 7. Results of trapping experiment.

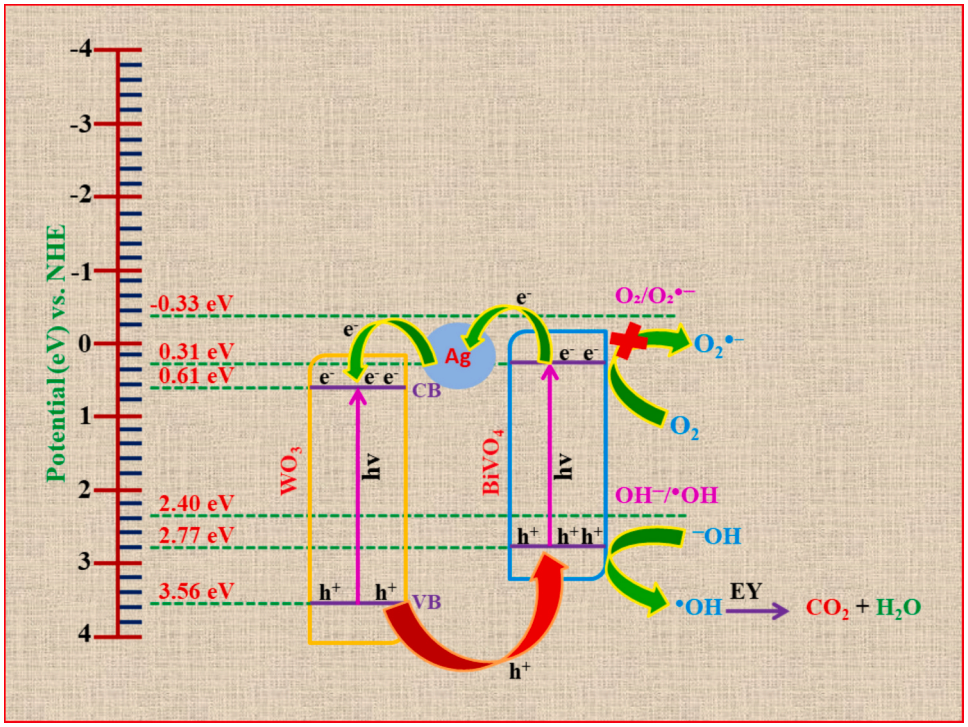

Fig. 8. Proposed mechanism of photocatalytic degradation of eosin yellow (EY) dye by ABvW. (For interpretation of the references to colour in this figure legend, the reader is referred to the web version of this article.)

7. Conclusion

In this study, we successfully synthesized an Ag-WO_3/$BiVO_4$ (ABvW) heterostructure nanocomposite, along with pure $BiVO_4$ and WO_3 samples. The materials were characterized using various spectroscopic and electron microscopic techniques. The photocatalytic performance of the synthesized samples was evaluated by monitoring the degradation of eosin yellow (EY) under LED light illumination. Photocatalytic results revealed that ABvW exhibited the highest efficiency among the samples. This superior performance is attributed to the improved specific surface area, which provides a greater number of active sites for dye adsorption, as well as the effective suppression of charge recombination between photogenerated electrons and holes. The stability of the most efficient ABvW photocatalyst was confirmed through recyclability tests, which showed only a 6 % decrease in efficiency after four cycles, indicating excellent long-term stability. We compared the efficiency of our ABvW catalysts with those from other studies, evaluating metrics such as quantum yield (QY), space-time yield (STY), and figure of merit (FOM). Our results indicate that our sample demonstrates the highest efficiency among those analyzed.

CRediT authorship contribution statement

Suresh Kumar Pandey: Writing – original draft, Visualization, Validation, Methodology, Investigation, Formal analysis, Data curation, Conceptualization. **Prerna Sarwan:** Validation, Investigation, Formal analysis, Data curation. **Dhanesh Tiwary:** Writing – review & editing, Supervision, Funding acquisition, Conceptualization. **Mohammad Salman:** Writing – original draft, Visualization.

Declaration of competing interest

The authors declare that they have no financial or personal relationships that could be perceived as potential conflicts of interest in relation to the work presented in this paper.

Acknowledgments

The authors would like to express their gratitude to the Central Instrument Facility (CIF) at the Indian Institute of Technology (BHU), Varanasi for providing the necessary instrumentation support.

Appendix A. Supplementary data

Supplementary data to this article can be found online at https://doi.org/10.1016/j.jwpe.2025.107216.

Data availability

Data will be made available on request.

References

[1] J.C. Murillo-Sierra, A. Hernández-Ramírez, L. Hinojosa-Reyes, J.L. Guzmán-Mar, A review on the development of visible light-responsive WO3-based photocatalysts for environmental applications, Chemical Engineering Journal Advances 5 (2021) 100070, https://doi.org/10.1016/j.ceja.2020.100070.
[2] A. Hameed, V. Gombac, T. Montini, M. Graziani, P. Fornasiero, Synthesis, characterization and photocatalytic activity of NiO–Bi2O3 nanocomposites, Chem. Phys. Lett. 472 (2009) 212–216, https://doi.org/10.1016/j.cplett.2009.03.017.
[3] S.K. Pandey, P.K. Mishra, D. Tiwary, Enhanced photocatalytic performance of NiS/ZnO nanocomposite for the remediation of PNP and RhB dye, J. Environ. Chem. Eng. 10 (2022) 107459, https://doi.org/10.1016/j.jece.2022.107459.
[4] A. Saravanan, P.S. Kumar, D.-V.N. Vo, P.R. Yaashikaa, S. Karishma, S. Jeevanantham, B. Gayathri, V.D. Bharathi, Photocatalysis for removal of environmental pollutants and fuel production: a review, Environ. Chem. Lett. 19 (2021) 441–463, https://doi.org/10.1007/s10311-020-01077-8.
[5] M. Rani, U. Shanker, Photocatalytic degradation of toxic phenols from water using bimetallic metal oxide nanostructures, Colloids Surf. A Physicochem. Eng. Asp. 553 (2018) 546–561, https://doi.org/10.1016/j.colsurfa.2018.05.071.
[6] M. Hojamberdiev, B. Czech, A.C. Göktaş, K. Yubuta, Z.C. Kadirova, SnO2@ZnS photocatalyst with enhanced photocatalytic activity for the degradation of selected pharmaceuticals and personal care products in model wastewater, J. Alloys Compd. 827 (2020) 154339, https://doi.org/10.1016/j.jallcom.2020.154339.
[7] K. Zhang, J. Deng, Y. Liu, S.X. and H. Dai, K. Zhang, J. Deng, Y. Liu, S.X. and H. Dai, Photocatalytic Removal of Organics over BiVO4-Based Photocatalysts, in: Semiconductor Photocatalysis - Materials, Mechanisms and Applications, IntechOpen, 2016. doi:https://doi.org/10.5772/62745.

[8] D. Monga, P. Kaur, B. Singh, Microbe mediated remediation of dyes, explosive waste and polyaromatic hydrocarbons, pesticides and pharmaceuticals, Current Research in Microbial Sciences 3 (2022) 100092, https://doi.org/10.1016/j.crmicr.2021.100092.
[9] H. Du, W. Pu, Y. Wang, K. Yan, J. Feng, J. Zhang, C. Yang, J. Gong, Synthesis of BiVO4/WO3 composite film for highly efficient visible light induced photoelectrocatalytic oxidation of norfloxacin, J. Alloys Compd. 787 (2019) 284–294, https://doi.org/10.1016/j.jallcom.2019.01.390.
[10] B.J. Singh, A. Chakraborty, R. Sehgal, A systematic review of industrial wastewater management: evaluating challenges and enablers, J. Environ. Manag. 348 (2023) 119230, https://doi.org/10.1016/j.jenvman.2023.119230.
[11] S. Sun, W. Wang, S. Zeng, M. Shang, L. Zhang, Preparation of ordered mesoporous ag/WO3 and its highly efficient degradation of acetaldehyde under visible-light irradiation, J. Hazard. Mater. 178 (2010) 427–433, https://doi.org/10.1016/j.jhazmat.2010.01.098.
[12] M. Gao, L. You, L. Guo, T. Li, Fabrication of a novel polyhedron-like WO3/Ag2CO3 p-n junction photocatalyst with highly enhanced photocatalytic activity, J. Photochem. Photobiol. A Chem. 374 (2019) 206–217, https://doi.org/10.1016/j.jphotochem.2019.01.022.
[13] A.N. Ejhieh, M. Khorsandi, Photodecolorization of Eriochrome black T using NiS–P zeolite as a heterogeneous catalyst, J. Hazard. Mater. 176 (2010) 629–637, https://doi.org/10.1016/j.jhazmat.2009.11.077.
[14] X. Song, Q. Yang, M. Yin, D. Tang, L. Zhou, Highly efficient pollutant removal of graphitic carbon nitride by the synergistic effect of adsorption and photocatalytic degradation, RSC Adv. 8 (2018) 7260–7268, https://doi.org/10.1039/C7RA11467B.
[15] S. Mohammed Harshulkhan, K. Janaki, G. Velraj, R. Sakthi Ganapathy, S. Krishnaraj, Structural and optical properties of ag doped tungsten oxide (WO3) by microwave-assisted chemical route, J. Mater. Sci. Mater. Electron. 27 (2016) 3158–3163, https://doi.org/10.1007/s10854-015-4138-1.
[16] L. Xie, T. Du, J. Wang, Y. Ma, Y. Ni, Z. Liu, L. Zhang, C. Yang, J. Wang, Recent advances on heterojunction-based photocatalysts for the degradation of persistent organic pollutants, Chem. Eng. J. 426 (2021) 130617, https://doi.org/10.1016/j.cej.2021.130617.
[17] Y. Lim, S.Y. Lee, D. Kim, M.-K. Han, H.S. Han, S.H. Kang, J.K. Kim, U. Sim, Y. I. Park, Expanded solar absorption spectrum to improve photoelectrochemical oxygen evolution reaction: synergistic effect of upconversion nanoparticles and ZnFe2O4/TiO2, Chem. Eng. J. 438 (2022) 135503, https://doi.org/10.1016/j.cej.2022.135503.
[18] M. Ijaz, M. Zafar, Titanium dioxide nanostructures as efficient photocatalyst: Progress, challenges and perspective, Int. J. Energy Res. 45 (2021) 3569–3589, https://doi.org/10.1002/er.6079.
[19] A. Zhang, J. Zhang, Synthesis and characterization of ag/BiVO4 composite photocatalyst, Appl. Surf. Sci. 256 (2010) 3224–3227, https://doi.org/10.1016/j.apsusc.2009.12.009.
[20] M.-L. Guan, D.-K. Ma, S.-W. Hu, Y.-J. Chen, S.-M. Huang, From hollow olive-shaped BiVO4 to n−p Core−Shell BiVO4@Bi2O3 microspheres: controlled synthesis and enhanced visible-light-responsive photocatalytic properties, Inorg. Chem. 50 (2011) 800–805, https://doi.org/10.1021/ic101961z.
[21] H. Xu, H. Li, C. Wu, J. Chu, Y. Yan, H. Shu, Preparation, characterization and photocatalytic activity of transition metal-loaded BiVO4, Mater. Sci. Eng. B 147 (2008) 52–56, https://doi.org/10.1016/j.mseb.2007.11.011.
[22] M. Sharma, D. Sajwan, A. Gouda, A. Sharma, V. Krishnan, Recent progress in defect-engineered metal oxides for photocatalytic environmental remediation, Photochem. Photobiol. 100 (2024) 830–896, https://doi.org/10.1111/php.13959.
[23] L. Aamir, Novel p-type ag-WO3 nano-composite for low-cost electronics, photocatalysis, and sensing: synthesis, characterization, and application, J. Alloys Compd. 864 (2021) 158108, https://doi.org/10.1016/j.jallcom.2020.158108.
[24] O. Samuel, M.H.D. Othman, R. Kamaludin, O. Sinsamphanh, H. Abdullah, M. H. Puteh, T.A. Kurniawan, WO3–based photocatalysts: a review on synthesis, performance enhancement and photocatalytic memory for environmental applications, Ceram. Int. 48 (2022) 5845–5875, https://doi.org/10.1016/j.ceramint.2021.11.158.
[25] W. Zhu, J. Liu, S. Yu, Y. Zhou, X. Yan, Ag loaded WO3 nanoplates for efficient photocatalytic degradation of sulfanilamide and their bactericidal effect under visible light irradiation, J. Hazard. Mater. 318 (2016) 407–416, https://doi.org/10.1016/j.jhazmat.2016.06.066.
[26] M. Munir Sajid, H. Zhai, M.A. Iqbal, N. Akhtar Shad, Y. Javed, A. Raza Ishaq, B. Abd Alreda, K. Morsy, J.R. Choi, Experimental insights on the synthesis and characteristics of Fe1−xBixVO4 photocatalysts for efficient environmental and electrical applications, Arab. J. Chem. 16 (2023) 104986, https://doi.org/10.1016/j.arabjc.2023.104986.
[27] J. Safaei, H. Ullah, N.A. Mohamed, M.F. Mohamad Noh, M.F. Soh, A.A. Tahir, N. Ahmad Ludin, M.A. Ibrahim, W.N.R. Wan Isahak, M.A. Mat Teridi, Enhanced photoelectrochemical performance of Z-scheme g-C3N4/BiVO4 photocatalyst, Appl. Catal. B Environ. 234 (2018) 296–310, https://doi.org/10.1016/j.apcatb.2018.04.056.
[28] S. Xu, D. Fu, K. Song, L. Wang, Z. Yang, W. Yang, H. Hou, One-dimensional WO3/BiVO4 heterojunction photoanodes for efficient photoelectrochemical water splitting, Chem. Eng. J. 349 (2018) 368–375, https://doi.org/10.1016/j.cej.2018.05.100.
[29] P. Chatchai, Y. Murakami, S. Kishioka, A.Y. Nosaka, Y. Nosaka, Efficient photocatalytic activity of water oxidation over WO3/BiVO4 composite under visible light irradiation, Electrochim. Acta 54 (2009) 1147–1152, https://doi.org/10.1016/j.electacta.2008.08.058.
[30] X. Fan, Q. Chen, F. Zhu, T. Wang, B. Gao, L. Song, J. He, Preparation of surface dispersed WO3/BiVO4 heterojunction arrays and their Photoelectrochemical performance for water splitting, Molecules 29 (2024) 372, https://doi.org/10.3390/molecules29020372.
[31] Q. Deng, X. Duan, D.H.L. Ng, H. Tang, Y. Yang, M. Kong, Z. Wu, W. Cai, G. Wang, Ag nanoparticle decorated Nanoporous ZnO microrods and their enhanced photocatalytic activities, ACS Appl. Mater. Interfaces 4 (2012) 6030–6037, https://doi.org/10.1021/am301682g.
[32] H. Salari, Efficient photocatalytic degradation of environmental pollutant with enhanced photocarrier separation in novel Z-scheme a-MnO2 nanorod/a-MoO3 nanocomposites, J. Photochem. Photobiol. A Chem. 401 (2020) 112787, https://doi.org/10.1016/j.jphotochem.2020.112787.
[33] B. Chai, M. Xu, J. Yan, Z. Ren, Remarkably enhanced photocatalytic hydrogen evolution over MoS2 nanosheets loaded on uniform CdS nanospheres, Appl. Surf. Sci. 430 (2018) 523–530, https://doi.org/10.1016/j.apsusc.2017.07.292.
[34] Y. Liu, R. Liu, C. Liu, S. Luo, L. Yang, F. Sui, Y. Teng, R. Yang, Q. Cai, Enhanced photocatalysis on TiO2 nanotube arrays modified with molecularly imprinted TiO2 thin film, J. Hazard. Mater. 182 (2010) 912–918, https://doi.org/10.1016/j.jhazmat.2010.07.007.
[35] R.A. Carcel, L. Andronic, A. Duta, Photocatalytic activity and stability of TiO2 and WO3 thin films, Mater. Charact. 70 (2012) 68–73, https://doi.org/10.1016/j.matchar.2012.04.021.
[36] H. Anwer, A. Mahmood, J. Lee, K.-H. Kim, J.-W. Park, A.C.K. Yip, Photocatalysts for degradation of dyes in industrial effluents: opportunities and challenges, Nano Res. 12 (2019) 955–972, https://doi.org/10.1007/s12274-019-2287-0.
[37] H. Anwer, J.-W. Park, Synthesis and characterization of a heterojunction rGO/ZrO2/Ag3PO4 nanocomposite for degradation of organic contaminants, J. Hazard. Mater. 358 (2018) 416–426, https://doi.org/10.1016/j.jhazmat.2018.07.019.
[38] K. Vikrant, C.M. Park, K.-H. Kim, S. Kumar, E.-C. Jeon, Recent advancements in photocatalyst-based platforms for the destruction of gaseous benzene: performance evaluation of different modes of photocatalytic operations and against adsorption techniques, J. Photochem. Photobiol. C Photchem. Rev. 41 (2019) 100316, https://doi.org/10.1016/j.jphotochemrev.2019.08.003.
[39] N. Raza, W. Raza, H. Gul, M. Azam, J. Lee, K. Vikrant, K.-H. Kim, Corrigendum for "Solar-light-active silver phosphate/titanium dioxide/silica heterostructures for photocatalytic removal of organic dye"[J. Clean. Prod. 254 (2020) 120031], J. Clean. Prod. 281 (2021). https://repository.hanyang.ac.kr/handle/20.500.11754/176747 (accessed October 31, 2024).
[40] M.C.R. Silva, S. Castro-Lopes, A.G. Jerônimo, R. Barbosa, A. Lins, P. Trigueiro, B. C. Viana, F.P. Araujo, J.A. Osajima, R.R. Peña-Garcia, Green synthesis of Er-doped ZnO nanoparticles: an investigation on the methylene blue, Eosin, and Ibuprofen Removal by Photodegradation, Molecules 29 (2024) 391, https://doi.org/10.3390/molecules29020391.
[41] S. Jayasankari, A. Pramothkumar, P. Mani, Facile synthesis and characterization of ZnO NPs, ZnO/CdO and ZnO/SnO2 nanocomposites for photocatalytic degradation of eosin yellow and direct blue 15 under UV light irradiation, J. Mater. Sci. Mater. Electron. 33 (2022) 9858–9874.
[42] A.A. Abdel-Khalek, S.A. Mahmoud, A.H. Zaki, Visible light assisted photocatalytic degradation of crystal violet, bromophenol blue and eosin Y dyes using AgBr-ZnO nanocomposite, Environmental Nanotechnology, Monitoring & Management 9 (2018) 164–173, https://doi.org/10.1016/j.enmm.2018.03.002.
[43] C.K. Bandoh, B.Y. Danu, E.S. Agorku, F.K. Ampong, R.K. Nkum, The effect of cobalt-doped ZnO-g-C3N4 heterostructures on photocatalytic degradation of eosin yellow dye in water under simulated solar light, Results in Materials 21 (2024) 100515, https://doi.org/10.1016/j.rinma.2023.100515.
[44] V. Ramasamy Raja, D.R. Rosaline, A. Suganthi, M. Rajarajan, Facile sonochemical synthesis of Zn2SnO4-V2O5 nanocomposite as an effective photocatalyst for degradation of eosin yellow, Ultrason. Sonochem. 44 (2018) 310–318, https://doi.org/10.1016/j.ultsonch.2018.02.043.
[45] W.W. Anku, S.O.-B. Oppong, S.K. Shukla, E.S. Agorku, P.P. Govender, Cobalt doped ZrO2 decorated multiwalled carbon nanotube: a promising nanocatalyst for photodegradation of indigo carmine and eosin Y dyes, Prog. Nat. Sci.: Mater. Int. 26 (2016) 354–361, https://doi.org/10.1016/j.pnsc.2016.06.007.
[46] D. Ayodhya, G. Veerabhadram, Hydrothermally generated and highly efficient sunlight responsive SiO2 and TiO2 capped Ag2S nanocomposites for photocatalytic degradation of organic dyes, journal of environmental, Chem. Eng. 6 (2018) 311–324, https://doi.org/10.1016/j.jece.2017.11.071.
[47] D. Rani Rosaline, S.S.R. Inbanathan, A. Suganthi, M. Rajarajan, G. Kavitha, R. Srinivasan, H.H. Hegazy, A. Umar, H. Algarni, E. Manikandan, Visible-light driven photocatalytic degradation of eosin yellow (EY) dye based on NiO-WO3 nanoparticles, J. Nanosci. Nanotechnol. 20 (2020) 924–933, https://doi.org/10.1166/jnn.2020.16898.
[48] S. Siva Kumar, V. Ranga Rao, G. Nageswara Rao, Effect of silver impregnation on efficiency of ZnO for photocatalytic degradation of eosin Y, Proc. Natl. Acad. Sci., India, Sect. A Phys. Sci. 83 (2013) 7–14, https://doi.org/10.1007/s40010-012-0063-3.
[49] S.Y. Janbandhu, U. Patra, G.K. Sukhadeve, R. Kumar, R.S. Gedam, Photocatalytic performance of glasses embedded with ag-TiO2 quantum dots on photodegradation of indigo carmine and eosin Y dyes in sunlight, Inorg. Chem. Commun. 148 (2023) 110317, https://doi.org/10.1016/j.inoche.2022.110317.
[50] M.S. Song, R.P. Patil, M.A. Mahadik, Y.J. Jo, J.-H. Park, W.-S. Chae, S.H. Choi, H. H. Lee, J.S. Jang, Microwave-assisted CuO-modified porous ZnO nanosheet for photocatalytic degradation of organic pollutants and antibacterial inactivation,

J. Environ. Chem. Eng. 12 (2024) 114453, https://doi.org/10.1016/j.jece.2024.114453.

[51] K. Vignesh, A. Suganthi, M. Rajarajan, R. Sakthivadivel, Visible light assisted photodecolorization of eosin-Y in aqueous solution using hesperidin modified TiO2 nanoparticles, Appl. Surf. Sci. 258 (2012) 4592–4600, https://doi.org/10.1016/j.apsusc.2012.01.035.

[52] R. Tehreem, M. Awais, S. Khursheed, F. Rehman, D. Hussain, Y.S. Mok, G. U. Siddiqui, Synthesis of efficient light harvesting Cr, N co-doped TiO2 nanoparticles for enhanced visible light photocatalytic degradation of xanthene dyes; eosin yellow and rose bengal, Environ. Sci. Pollut. Res. 30 (2023) 92621–92635, https://doi.org/10.1007/s11356-023-28701-8.